

Characterization of a Far-Infrared Kinetic Inductance Detector Prototype for PRIMA

Steven Hailey-Dunsheath, Sven van Berkel, Andrew E. Beyer, Logan Foote, Reinier M. J. Janssen, Henry G. LeDuc, Pierre M. Echternach, Charles M. Bradford, Jochem J.A. Baselmans, Shahab Dabironezare, Peter K. Day, Nicholas F. Cothard, Jason Glenn

Abstract—The PRoBe far-Infrared Mission for Astrophysics (PRIMA) is under study as a potential far-IR space mission, featuring actively cooled optics, and both imaging and spectroscopic instrumentation. To fully take advantage of the low background afforded by a cold telescope, spectroscopy with PRIMA requires detectors with a noise equivalent power (NEP) better than $1 \times 10^{-19} \text{ W Hz}^{-1/2}$. To meet this goal we are developing large format arrays of kinetic inductance detectors (KIDs) to work across the $25 - 250 \mu\text{m}$ range. Here we present the design and characterization of a single pixel prototype detector optimized for $210 \mu\text{m}$. The KID consists of a lens-coupled aluminum inductor-absorber connected to a niobium interdigitated capacitor to form a 2 GHz resonator. We have fabricated a small array with 28 KIDs, and we measure the performance of one of these detectors with an optical loading in the $0.01 - 300 \text{ aW}$ range. At low loading the detector achieves an NEP of $9 \times 10^{-20} \text{ W Hz}^{-1/2}$ at a 10 Hz readout frequency, and the lens-absorber system achieves a good optical efficiency. An extrapolation of these measurements suggest this detector may remain photon noise limited at up to 20 fW of loading, offering a high dynamic range for PRIMA observations of bright astronomical sources.

Index Terms—kinetic inductance detectors, PRIMA, far-infrared, ultra-low NEP.

S. Hailey-Dunsheath is with the California Institute of Technology, Pasadena, CA 91125 USA (e-mail: haileyds@caltech.edu)

I. INTRODUCTION

Far-infrared (far-IR; $25 - 250 \mu\text{m}$) spectroscopy and spectrophotometry are unique tools for studying the interiors of galaxies and forming planetary systems. Far-IR radiation readily escapes regions that are deeply obscured by dust at optical and near-infrared wavelengths, and far-IR measurements can provide quantitative metrics of star formation and black hole growth in distant galaxies, as well as the chemical constituents of protoplanetary disks as they evolve. Revolutionary advances are still possible with a modest space mission in the far-IR, because a platform that operates at the fundamental limits in the band between JWST and ALMA has not yet been fielded. We are developing the PRoBe far-Infrared Mission for Astrophysics (PRIMA [1])¹, a NASA concept that features a 2-m class telescope and optics cooled to below 5 K. With sufficiently-sensitive detectors, this cold telescope enables measurements limited by only the photon shot noise of the zodiacal and Galactic dust emission. The PRIMA FIRESS grating spectrometer has an $R \sim 130$ spectral

bin per detector pixel, and an estimated 20% optical efficiency into a $1 \text{ f}\lambda$ dual-polarization pixel. When looking toward the north ecliptic pole, this fundamental photon noise limit corresponds to a detector noise equivalent power (NEP) of $\approx 1 \times 10^{-19} \text{ W Hz}^{-1/2}$ in the $100 - 250 \mu\text{m}$ range.

Kinetic inductance detectors (KIDs) are poised to meet this demanding sensitivity requirement while also offering favorable system properties compatible with a modest space mission: operation temperature up to 150 mK, high multiplex factor, and low focal plane power dissipation. KIDs have demonstrated high yield in kilopixel arrays [2], [3], sufficient immunity to cosmic-ray interactions [4], [5], and have been fielded successfully in balloon instruments [6], [7]. The unique sensitivity requirements for a PRIMA-like mission have been demonstrated in antenna-coupled 1.5 THz ($200 \mu\text{m}$) devices [8], [9], setting the stage for proceeding with PRIMA for implementation this decade. Here we present a KID design developed specifically for PRIMA that uses a lens-coupled all aluminum multi-mode absorber architecture, building on the development of KID focal planes for the TIM and BLAST balloon experiments [3], [7], [10], [11]. Relative to an antenna-coupled (single-mode) approach, the multi-mode absorber coupling can scale to the shortest far-IR wavelengths, and offers increased versatility in the instrument design. This article focuses on a $210 \mu\text{m}$ KID that demonstrates an NEP below $10^{-19} \text{ W Hz}^{-1/2}$ at 10 Hz. We present the device design, measured performance, and validation of our KID sensitivity model, which allows confident prediction of in-flight performance with PRIMA. We have also designed and built 1008-pixel arrays using this pixel architecture. Early testing of these shows $>90\%$ resonator yield; sensitivity statistics and cosmic-ray response are presented in companion articles [5], [12].

II. DETECTOR DESIGN AND FABRICATION

A. Device Description

The layout of an individual KID is shown in Figure 1. Each pixel consists of a niobium interdigitated capacitor (IDC) connected to an aluminum inductor to form a parallel LC resonant circuit. The IDC uses $2 \mu\text{m}$ wide fingers with a $10 \mu\text{m}$ spacing, and the capacitor size is varied from pixel to pixel so each pixel will have a unique resonance frequency, allowing for a frequency multiplexed readout [12]. A niobium coplanar waveguide (CPW) structure meanders through the

¹www.prima.ipac.caltech.edu

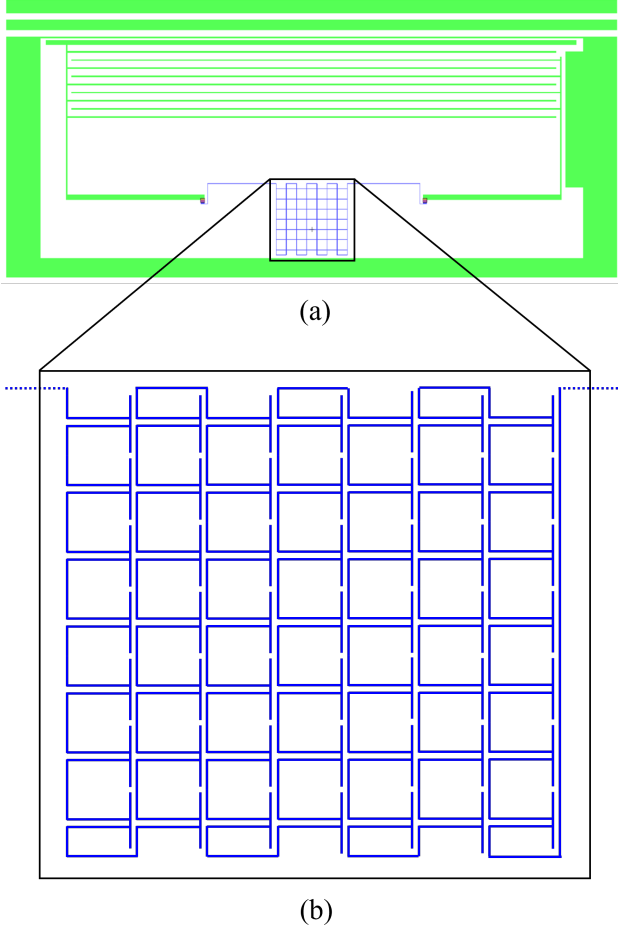


Fig. 1. Layout of a single KID. (a) Niobium features include the CPW readout line along the top of the figure, the IDC, and the surrounding ground plane (*green*). The inductor-absorber is aluminum (*blue*), and connects to the IDC through a niobium plug (*red*). (b) Schematic of the inductor-absorber highlighting the connections between individual unit cells. This drawing is not to scale – the gaps between traces have been exaggerated for clarity (see Figure 2).

device to capacitively couple the microwave readout signal to each individual pixel. A region of the ground plane extends to the edge of the IDC to provide a capacitive coupling, and a path to ground for the microwave current. The feedline and IDC are made from a sputter-deposited layer of niobium, and patterned using reactive ion etching. During etching, a resist mask patterned using optical stepper lithography is used to achieve the desired geometry. The aluminum inductor is defined by electron beam lithography and liftoff of a 30 nm thick sputtered aluminum layer. The connection between the niobium IDC and the aluminum inductor is accomplished by a niobium plug defined by photolithography. Prior to the niobium deposition the surface layer of aluminum oxide is stripped using ion milling to provide a good electrical contact between the capacitor and inductor. The device is fabricated on a 300 μm thick high resistivity float zone (HRFZ) grown silicon wafer to provide good transmission in the far-IR. This wafer is then glued to another HRFZ silicon wafer containing a lens array.

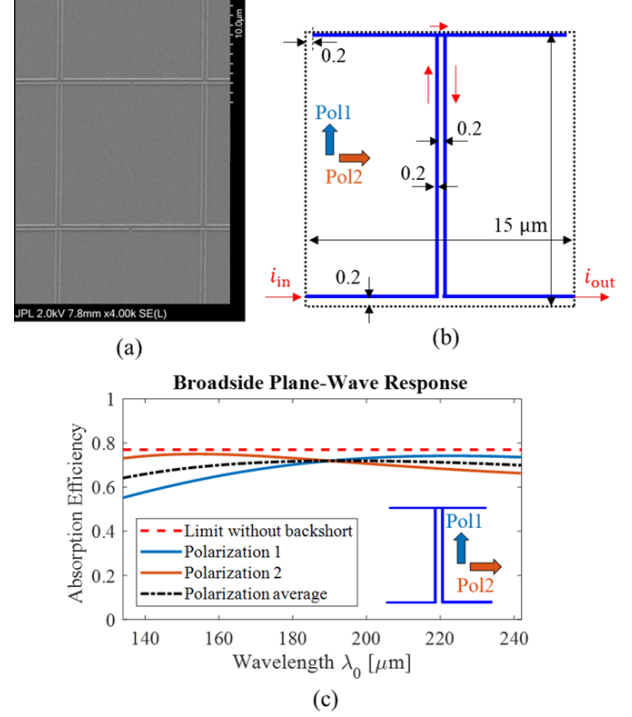


Fig. 2. Optimized II-absorber. Orientation is rotated by 90° with respect to Figure 1. (a) SEM picture, (b) schematic with dimensions, and (c) broadside plane wave response.

B. Absorber Design

The aluminum inductor, which is superconducting at microwave frequencies, doubles as an absorber at THz frequencies. A II-shaped absorber was optimized for absorbing signals from two orthogonal linear polarizations (Figure 2). When placed in a periodic grid and connected on the sides, this unit cell forms a single meandering inductor. The upper horizontal line of the II does not contribute to the inductance but improves absorption of the vertical polarization via capacitive coupling to the adjacent unit cell. The absorber unit cell is optimized using full-wave simulations considering infinite silicon and air half-spaces above and below the absorber, respectively. To simplify the fabrication and assembly, no quarter-wavelength backshort was used, which limits the potential absorption efficiency to approximately 77%. The aluminum was modeled with a sheet resistance of $R_s = 1.15 \Omega/\square$. A minimum line width and line separation of 0.2 μm was enforced, leading to a unit cell periodicity of 15 μm to achieve optimum absorber efficiency. The optimized absorber response for a broadside plane wave coming from the silicon is shown in Figure 2c. A polarization-averaged absorption efficiency of 70% was achieved over a broad band, close to the theoretical limit of 77% for an absorber without backshort².

²With no backshort the maximum absorption efficiency for normal incidence is $n/(1+n) = 0.77$ for silicon, assuming an index of refraction $n = 3.42$.

C. Lens Design and Optical Efficiency

The lens concentrates incident light from a large area onto a significantly smaller absorber, and greatly impacts the net optical efficiency. Maximizing the optical response of the detector requires minimizing the absorber volume. We have studied square absorbers in a 5x5 or 7x7 unit cell configuration, corresponding to aluminum volumes of $11.3 \mu\text{m}^3$ and $20.6 \mu\text{m}^3$, respectively. Both configurations use the same unit cell, shown in Figure 2b. The absorbers are comparable in size to a wavelength in silicon – $75 \mu\text{m}$ ($\approx 1.3\lambda$) or $105 \mu\text{m}$ ($\approx 1.8\lambda$) for $\lambda = 200 \mu\text{m}$, and therefore low focal ratio ($f/\#$) lenses are needed to minimize the spillover losses [13]. The minimum lens $f/\#$ possible was dictated by the minimum wafer thickness we were comfortable handling, which was $300 \mu\text{m}$ for the detector wafer and $200 \mu\text{m}$ at the thinnest points of the lens wafer. This leads to an extended hemispherical lens design with $f/\# = 0.745$. The simulated spillover efficiency at $\lambda = 200 \mu\text{m}$ with respect to the absorbers was 83% and 90% for the 5x5 and 7x7 grids, respectively.

Figure 3 shows the simulated optical efficiency of the lens-coupled absorber, assuming a broadside plane wave impinging on the lens surface. Simulations are performed in CST Microwave Studio using the finite-difference time-domain (FDTD) method. The efficiency is analyzed both with and without a Parylene-C ($\epsilon_r = 2.62$) quarter-wavelength anti-reflection (AR) coating. The measurements presented in this work are done with lens arrays without an AR-coating. The black lines in Figure 3 show the polarization-averaged efficiency, which is between 44% – 48% for the 5x5 absorber, and between 47% – 50% for the 7x7 absorber.

The red dashed lines in Figure 3 indicate the approximate theoretical limits to the optical efficiency, including the absence of a backshort ($\sim 77\%$ for a broadside plane wave), presence of an AR-coating ($\sim 70\%$ limit without coating³), and the simulated spillover of the focal plane field. This spillover efficiency is a function of wavelength and is calculated as the ratio of the power that is geometrically available to the finite sized absorber to the total power incident in the lens focal plane. These calculations are performed using an efficient quasi-analytical method [14]. At long wavelengths the absorbers become electrically small and the effective area can be larger than the geometrical area [15], such that the spillover efficiency as calculated here underestimates the true absorption efficiency. This effect is responsible for the drop in the theoretical absorption limits shown in Figure 3, which fall below the simulated efficiencies at long wavelengths, particularly for the smaller 5x5 unit cell absorber.

The 21x21 lens array used in this measurement was machined with laser ablation technology at Veldlaser⁴. SEM pictures of a portion of the array and zoom-in of the lens surface are shown in Figure 4. The surface profile of a full

³With no AR-coating the transmission efficiency from free space into the silicon lens for a normally-incident plane wave is $1 - (1 - n)^2 / (1 + n)^2 = 0.70$, assuming an index of refraction $n = 3.42$.

⁴<https://www.veldlaser.nl/en/>

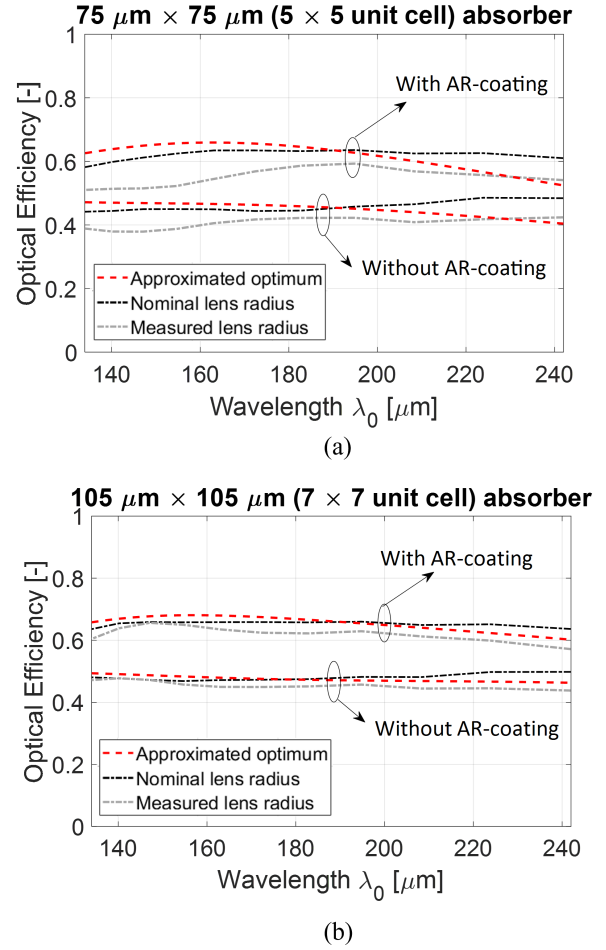


Fig. 3. Simulated optical efficiency of the lens-coupled absorbers, both with and without an AR coating. (a) Efficiency with the 5x5 absorber, and (b) with the 7x7 absorber. Polarization-averaged efficiencies with the nominal lens radius (black) and measured lens radius (grey) are compared with the theoretical limits (red dashed).

row of lenses (20 mm line scan with a $1 \mu\text{m}$ resolution) was measured using a Mitaka NH-5NS surface mapping tool⁵, indicating an increased (by $40.5 \mu\text{m}$) lens radius, and a surface roughness rms of $4.8 \mu\text{m}$. We repeated the full-wave simulations with the larger lens radius and found a reduction in the optical efficiency of up to 10% (Figure 3). The impact of the $4.8 \mu\text{m}$ rms surface roughness was estimated using the standard Ruze efficiency, adapted for refractive lenses [16], [17], which suggests an additional penalty of 12%. As a result of the larger radius and the finite surface roughness, the wavelength-averaged optical efficiency of the 7x7 unit cell absorber is simulated to be 40%.

In parallel with these initial measurements, NASA's Goddard Space Flight Center (GSFC) has developed 1008-pixel micro-lens arrays using etching via greyscale lithography. These arrays show excellent surface quality even for PRIMA's shortest wavelengths, as well as a short manufacture time [18]. They are now being manufactured in the PRIMA flight format,

⁵https://www.mitakakohki.co.jp/english/industry/nh_series/lineup/nh-5ns-.html

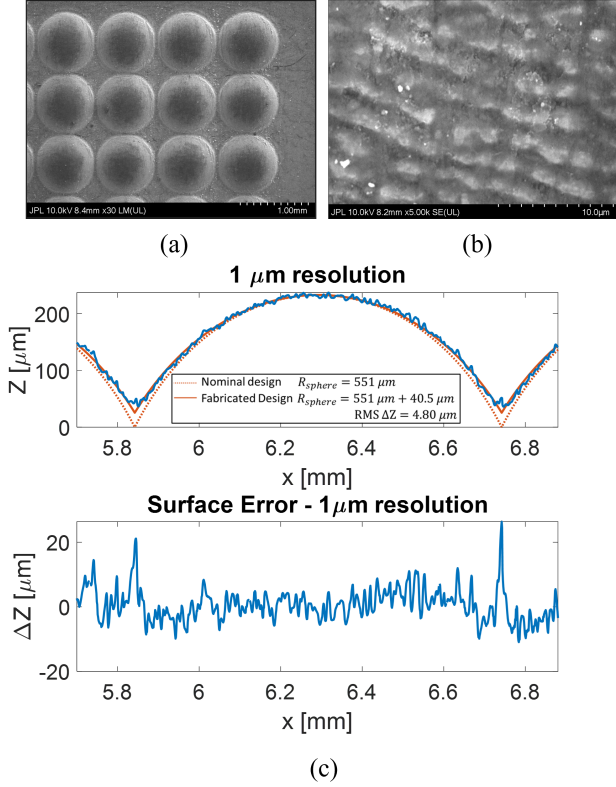


Fig. 4. Machined 21x21 lens array with low $f/\#$ lenses. (a) SEM of some lenses, (b) close-up SEM showing surface roughness, and (c) zoom-in of designed, measured, and simulated lens profile.

and are the baseline plan for PRIMA's KIDs.

III. EXPERIMENTAL SETUP

Figure 5 shows the optical setup. Radiation is generated by a variable temperature blackbody source that is mounted to the exterior of a cryogen-free dilution refrigerator's 4 K shield with low-thermal-conductivity flexures. The blackbody is thermally connected to the 4 K stage through copper braids chosen to provide a heat conductance that balances blackbody speed against thermal loading of the shield. A flange with a 3.8 cm opening limits the amount of blackbody radiation to avoid overheating the still shield. Radiation enters the still shield through a 4.6 cm diameter opening covered with a zytex filter, and the mixing chamber shield through a 500 μm diameter aperture. This small aperture reduces the optical throughput, which allows the desired optical power range ($10^{-21} - 4 \times 10^{-16}$ W) to be reached with the available blackbody temperatures (4 – 33 K). Additionally, the diffraction introduced by the 500 μm aperture ($= 2.5\lambda$ at 200 μm) causes a reasonably constant illumination level over the detector array. The aperture flange holds behind it a 2 THz low-pass filter. The detector array is located close to the mixing chamber plate inside a copper housing, which also secures in place a stack of five bandpass filters centered at 1.41 THz (213 μm). The peak transmission of the full filter stack is 44%, and the FWHM is 0.17 THz (Figure 5b). Both the still and mixing chamber

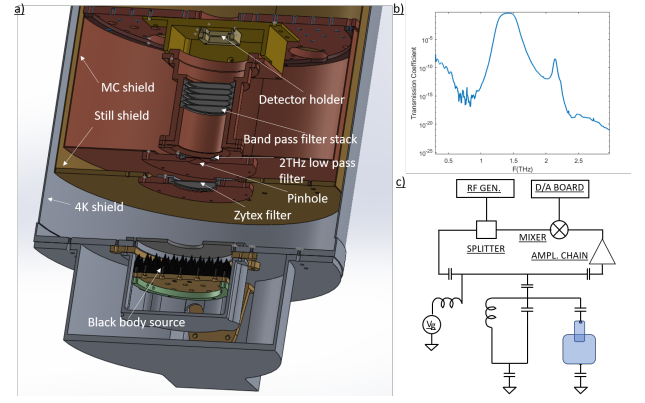


Fig. 5. (a) Optical setup. (b) Filter stack transmission coefficient as a function of frequency. Peak transmission is 44% at 1.42 THz, and FWHM is 0.17 THz. (c) Readout schematic.

shields are coated with a mixture of black epoxy and carbon black [19]. The blackbody radiation incident on the front of the lens is calculated by integrating the filtered source emission over the system passband (Figure 5b) as described in Ref. 13.

As shown in Figure 5c, measurements are performed by sending a microwave signal at the resonant frequency of the KID through a feedline that is capacitively coupled to the resonator. The transmitted signal is amplified by a cryogenic amplifier and a chain of warm amplifiers before being down-converted by an in-phase-quadrature (IQ) mixer. The down-converted in-phase and quadrature signals are digitized with a sample rate of 100kHz and saved separately.

IV. MEASUREMENTS

We cryogenically tested a wafer patterned with 14 large volume KIDs (with 7x7 unit cell inductors) and 14 small volume KIDs (with 5x5 unit cell inductors). The IDCs and coupling capacitors of these KIDs were designed to produce resonance frequencies in the 2 – 3 GHz range, and coupling quality factors of $Q_c = 10^4$. A total of 7 large volume KIDs were identified, and all of these showed a response to the cryogenic blackbody. We chose the resonator at $f_r = 2.1$ GHz with the strongest optical response for detailed study.

While only 7 of the 14 large volume KIDs on this wafer were identified, subsequent improvements to the fabrication procedure have increased this yield. The fabrication process employed on this wafer was designed for liftoff of small Al/AlOx/Al junctions, and not for a grid of closely spaced lines. We have improved the yield by 1) individually characterizing the bilayers in the liftoff process to input into 3D proximity correction software, along with the nominal grid design, for e-beam lithography exposure, and by 2) improving control of the undercut of the bottom layer. The fabrication yield on more recent large format arrays is $> 90\%$ [12].

A. Dark Measurements

We begin by characterizing the detector with the cryogenic blackbody set to 5.4K, which corresponds to a negligible incident power of 0.0096 aW at the front of the lens, effectively placing the detector in the dark. We perform a frequency sweep of the microwave source over the resonance with a drive power of $P_g = -98$ dBm at the detector, which is approximately 6 dB below the bifurcation power [20]. We fit the system-corrected microwave transmission using:

$$S_{21} = 1 - \frac{Q_r/Q_c (1 + j \tan(\phi))}{1 + 2jQ_r x}, \quad (1)$$

where $x = (f - f_r)/f_r$ is the fractional detuning away from the resonator frequency f_r , Q_r is the resonator quality factor, Q_c is the coupling quality factor, and the $\tan(\phi)$ term accounts for impedance mismatches along the transmission line [21], [22]. At $T = 125$ mK this fit yields $Q_r = 10^4$ and $Q_c = 1.1 \times 10^4$, close to the target value.

Transmission profiles as a function of the stage temperature for $T = 100 - 275$ mK are shown in Figure 6, and the estimated fractional frequency shift ($x = \delta f_r/f_r$) is shown in Figure 7. We fit this data with the standard Mattis-Bardeen expression [21]:

$$x_{\text{MB}} = -\frac{\alpha \gamma S_2(\omega)}{4N_0 \Delta_0} n_{\text{qp}}, \quad (2)$$

where α is the kinetic inductance fraction, Δ_0 is the gap energy, and $\gamma = 1$ is appropriate for the thin films used here. We adopt a density of states of $N_0 = 1.72 \times 10^{10} \mu\text{m}^{-3} \text{eV}^{-1}$ [23]. The quasiparticle number density n_{qp} is given by $n_{\text{th}} = 2N_0 \sqrt{2\pi k_B T \Delta_0} \exp(-\Delta_0/k_B T)$, and we also use the standard expression for $S_2(\omega)$ appropriate for a thermal quasiparticle distribution [21]:

$$S_2(\omega) = 1 + \sqrt{\frac{2\Delta_0}{\pi k_B T}} \exp\left(-\frac{\hbar\omega}{2k_B T}\right) I_0\left(\frac{\hbar\omega}{2k_B T}\right), \quad (3)$$

where $\omega = 2\pi f$. When using Equation 2 to model the data shown in Figure 7 we allow α and Δ_0 to vary, as discussed below.

The two models shown in Figure 7 are fits to $x(T)$ with α fixed at 0.95 and 0.50, respectively, and Δ_0 treated as a free parameter. For this temperature range α and Δ_0 are almost entirely degenerate, and additional information must be used to constrain these two parameters. Given the narrow 0.2 μm line width the kinetic inductance in the absorber is expected to be significantly larger than the geometric inductance, and electromagnetic simulations of the absorber with Sonnet⁶ indicate $\alpha \approx 0.95$. We thus adopt $\alpha = 0.95$ and $\Delta_0 = 0.245$ meV as our preferred model. Assuming the standard BCS relation between the gap energy and transition temperature ($\Delta_0 = 1.76 k_B T_c$) this corresponds to $T_c = 1.61$ K.

With $\alpha = 0.50$ the best fit value of Δ_0 is 0.231 meV, only $\approx 6\%$ lower than in our preferred model. This value of α would

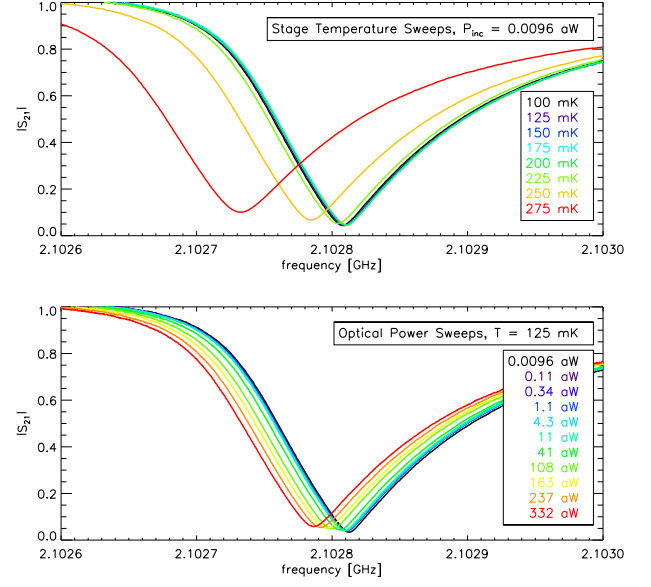


Fig. 6. System-corrected microwave transmission profiles as a function of stage temperature for fixed optical loading (top), and as a function of optical loading at fixed stage temperature (bottom).

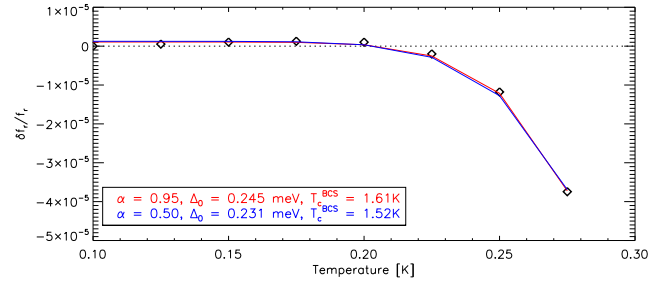


Fig. 7. Fractional frequency shift vs. stage temperature for a dark measurement, along with fits to $x = \delta f_r/f_r$ for a range of fixed α and variable Δ_0 . Models are $x = x_{\text{MB}} + \delta x$ for a zero temperature offset δx . The T_c is computed following the BCS relation $\Delta_0 = 1.76 k_B T_c$.

be significantly lower than expected from the simulations, and also lower than the values of α obtained in other narrow line aluminum inductors [10], [11], [24]. We consider this a conservative lower limit to the kinetic inductance fraction, and $\Delta_0 = 0.231$ meV a corresponding lower limit to the gap energy.

We stress that while these estimates of α and Δ_0 contain some uncertainty, precise values of these parameters are not required to measure the detector sensitivity. The calculation of the detector NEP and optical efficiency presented in Section IV-C does not require any knowledge of α , and is only weakly dependent on the adopted value of Δ_0 through Equation 9. We discuss this dependence more fully in Section IV-C.

B. Optical Measurements

We measure the optical response of this KID by fixing the stage temperature at 125 mK and running the cryogenic

⁶<https://www.sonnetsoftware.com/>

blackbody between 5.4–33.4 K, corresponding to an incident power range of $P_{\text{inc}} = 0.0096 - 332$ aW. The resultant resonator profiles are shown in the bottom panel of Figure 6, and the fractional frequency shift as a function of optical loading is shown in Figure 8.

If the quasiparticle generation rate due to the absorption of microwave readout power may be neglected, the change in the fractional frequency shift with respect to the change in incident power (P_{inc}) may be written as [21]:

$$\frac{dx}{dP_{\text{inc}}} = \eta_{\text{opt}} \frac{\alpha \gamma S_2(\omega)}{4N_0 \Delta_0} \frac{\eta_{\text{pb}} \tau_{\text{max}}}{\Delta_0 V} \quad (4a)$$

$$\left[\left(1 + \frac{n_{\text{th}}}{n^*} \right)^2 + \frac{2\eta_{\text{pb}} \eta_{\text{opt}} P_{\text{inc}} \tau_{\text{max}}}{n^* \Delta_0 V} \right]^{-1/2} \\ = R_0 \left[1 + \frac{P_{\text{inc}}}{P_0} \right]^{-1/2}, \quad (4b)$$

where we have introduced:

$$R_0 = \eta_{\text{opt}} \frac{\alpha \gamma S_2(\omega)}{4N_0 \Delta_0} \frac{\eta_{\text{pb}} \tau_{\text{max}}}{\Delta_0 V} \left(1 + \frac{n_{\text{th}}}{n^*} \right)^{-1} \quad (5a)$$

$$P_0 = \frac{n^* \Delta_0 V}{2\eta_{\text{pb}} \eta_{\text{opt}} \tau_{\text{max}}} \left(1 + \frac{n_{\text{th}}}{n^*} \right)^2. \quad (5b)$$

In these equations η_{opt} is the optical efficiency of the lens and absorber, such that the power absorbed in the detector is $P_{\text{abs}} = \eta_{\text{opt}} P_{\text{inc}}$. The quantity η_{pb} is the pair-breaking efficiency, defined as the fraction of the photon energy that breaks Cooper pairs, and V is the inductor volume. We adopt the common empirical description of the quasiparticle lifetime: $\tau_{\text{qp}} = \tau_{\text{max}}(1 + n_{\text{qp}}/n^*)^{-1}$, where n_{qp} is the quasiparticle number density at the given optical load, and τ_{max} and n^* are constants determined by the film properties.

In Equation 5, P_0 is constant with incident power and R_0 depends on the optical loading only through the parameter $S_2(\omega)$, which depends on the quasiparticle energy distribution. We estimate that $S_2(\omega)$ varies by only $\approx 10\%$ for the range of optical loading considered here. Neglecting this variation and treating R_0 as a constant, we may integrate Equation 4 to find:

$$x(P_{\text{inc}}) - x(P_{\text{inc}} = 0) = 2R_0 P_0 \left[\left(1 + \frac{P_{\text{inc}}}{P_0} \right)^{1/2} - 1 \right]. \quad (6)$$

A fit to the data in Figure 8 with this approach yields $R_0 = 7.6 \times 10^{10} \text{ W}^{-1}$ and $P_0 = 35.5$ aW (see Figure 8 inset).

At each optical load we obtain a 20 second time stream of IQ data at fixed tone frequency, and calculate the fractional frequency noise power spectral density (PSD), S_{xx} , shown in Figure 9. Focusing on sampling frequencies >10 Hz, we see at low optical loading the PSD is dominated by a power law component consistent with two-level system (TLS) noise [25], while at high optical loading the white photon noise dominates. The white noise component rolls off with a knee frequency of $\approx 0.4 - 1$ kHz, which is well below the ≈ 100 kHz resonator ring-down frequency ($f_{\text{ring}} = f_r/2Q_r$), or the ≈ 50 kHz roll-off due to the warm electronics filter, and we

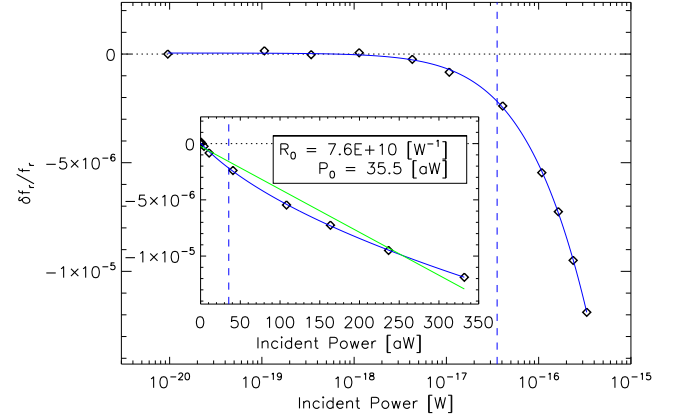


Fig. 8. Fractional frequency shift vs. incident optical power, along with a fit (blue) for Equation 6. Vertical dashed line shows the fitted value of the parameter P_0 . Inset shows the same on a linear scale, along with the result of a fit for a constant responsivity (green) for comparison.

attribute this knee to the quasiparticle lifetime. We fit the resonator contribution to the measured PSD at $f > 10$ Hz using:

$$S_{\text{xx}} = \frac{A f^{-0.25} + B}{1 + (2\pi f \tau_{\text{qp}})^2} + \frac{C}{1 + (2\pi f \tau_c)^2}, \quad (7)$$

where A represents the amplitude of the $1/f$ term, which we find is well described by an $f^{-0.25}$ power law, and B is the white noise term. We find evidence for a second white noise component in excess of the electronics noise, and account for this with the second term in Equation 7. Typical values here are $C = 1 \times 10^{-17} \text{ Hz}^{-1}$, and $\tau_c = 40 \mu\text{s}$ (corresponding to a knee frequency $f_c = 4$ kHz). The bottom panel of Figure 9 shows the fitted white noise amplitude (B), the $1/f$ noise amplitude at 10 Hz ($A \times 10^{-0.25}$), and τ_{qp} . At incident power levels above 1 aW there is sufficient photon noise to obtain a fit to τ_{qp} , and we estimate τ_{qp} decreases from 400 μs at 1.1 aW to 148 μs at 332 aW.

The frequency response to optical power may be used to provide an additional constraint on the quasiparticle lifetime. With the assumption that the changing slope dx/dP_{inc} seen in Figure 8 is due primarily to the change in τ_{qp} , we expect that the two quantities are proportional. Making use of Equation 4, we may express this as $\tau_{\text{qp}} \propto [1 + P_{\text{inc}}/P_0]^{-1/2}$. Normalizing this equation to the absolute value of $\tau_{\text{qp}} = 148 \mu\text{s}$ at $P_{\text{inc}} = 332$ aW measured from fitting the PSD roll-off, and adopting $P_0 = 35.5$ aW from the analysis of the data in Figure 8, we construct a model for τ_{qp} as a function of P_{inc} . This is shown as the green curve in Figure 9 (bottom). We find that this model is consistent with the values of τ_{qp} estimated by fitting the PSD roll-off, and indicates that τ_{qp} saturates at 400–500 μs as the optical load drops below 1 aW.

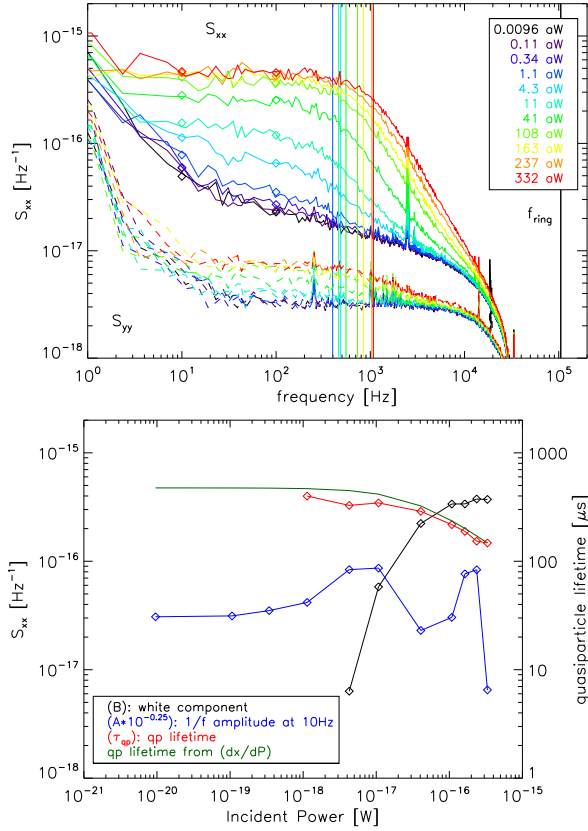


Fig. 9. (top) Fractional frequency noise over a range of optical loads, with electrical noise spikes at 60Hz and harmonics removed. Noise measured orthogonal to the phase direction shown as dashed lines (S_{yy}). Vertical lines indicate the fitted roll-off of the resonator component, and thick line at 100 kHz indicates the resonator ring-down frequency. (bottom) Fitting results of the PSDs using Equation 7. The quasiparticle lifetime estimated from the shape of dx/dP_{inc} is overplotted (green).

C. Noise Equivalent Power

With the electrical noise and response to incident power measured, we may compute the NEP referenced to power incident on the front of the lens as:

$$\text{NEP}_{\text{inc}} = \sqrt{S_{xx}} \left(\frac{dx}{dP_{\text{inc}}} \right)^{-1} \sqrt{1 + (2\pi f \tau_{\text{qp}})^2}. \quad (8)$$

In Section IV-B we used a detailed detector model to develop an expression for dx/dP_{inc} , but then grouped terms to arrive at a simple 2-parameter model of $x(P_{\text{inc}})$ (Equations 4, 5, and 6. This model provides an excellent match to the data (Figure 8), and we consider the resulting description of dx/dP_{inc} to be comparable to what would be obtained from an interpolation or other purely phenomenological description of the data in Figure 8). We use the measured S_{xx} in Equation 8, and consider the first two terms of this equation to be directly obtained from the data, with minimal influence of any model assumptions.

The third term in Equation 8 describes the reduced response at high sampling frequencies due to the finite τ_{qp} . As

described in Section IV-B this parameter is obtained through fits to the noise PSDs, supplemented by an extrapolation of the shape of dx/dP_{inc} to low optical powers. We adopt a value of $\tau_{\text{qp}} = 415 \mu\text{s}$ in the low-loading limit, but acknowledge some uncertainty in this number. Changes to this τ_{qp} will have little impact on the NEP at sampling frequencies of 10 – 100 Hz, and hence on the inferred optical efficiency (Figure 10), but will determine how quickly the NEP degrades at higher frequencies (Figure 11).

At high optical loading our noise is dominated by photon generation-recombination (GR) noise, and we may use the method developed by Ref. 26 to compute the optical efficiency η_{opt} , and with it the NEP referenced to absorbed power. For background limited operation the photon-limited NEP is:

$$\text{NEP}_{\gamma}^2 = 2h\nu P_{\text{abs}} \left(1 + n_0 + \frac{2\Delta_0}{h\nu\eta_{\text{pb}}} \right), \quad (9)$$

where the first term is the photon (generation) shot noise, the second term represents wave noise (for a photon occupation number n_0 in the detector), and the last term represents recombination noise. The wave noise term is negligible at these frequencies. For $\Delta_0 = 0.245 \text{ meV}$ and $\eta_{\text{pb}} = 0.5$ (Section V-C), this last term is $2\Delta_0/h\nu\eta_{\text{pb}} = 0.17$, indicating that recombination noise is a small contribution. The ratio of this expression for NEP_{γ} to the measured NEP_{inc} in the photon-noise limited regime is equal to $\sqrt{\eta_{\text{opt}}}$.

In Figure 10 we show the result of this analysis. Based on the photon noise comparison we estimate an optical efficiency of $\eta_{\text{opt}} = 90\%$. When referenced to absorbed power, the NEP at 10 Hz and 100 Hz sample frequencies approach $9 \times 10^{-20} \text{ W Hz}^{-1/2}$ and $6 \times 10^{-20} \text{ W Hz}^{-1/2}$, respectively, in the low loading limit. Using a smaller value of $\Delta_0 = 0.231 \text{ meV}$ (Section IV-A) will slightly reduce the recombination noise term in Equation 9, but will only reduce the inferred optical efficiency by $\sim 2\%$. In Figure 11 we show the NEP spectrum measured under the lowest optical loading ($P_{\text{abs}} = 0.0086 \text{ aW}$) as a function of sample frequency, calculated from Equation 8 with $\tau_{\text{qp}} = 415 \mu\text{s}$.

The 90% measured optical efficiency is a factor of 2.3 higher than the 40% absorption efficiency simulated for the 7x7 unit cell absorber and the as-built lens (Figure 3 and Section II-C). This discrepancy is not yet understood, but may be explained by any mechanism that increases the coupling of the detector to the cryogenic blackbody, such as an underestimate of the in-band filter transmission, the presence of out-of-band leakage, or scattering in the cryostat. We suggest that scattering within the detector package is the most likely cause of this elevated coupling, and highlight the possibility that some fraction of the light entering the detector package through an adjacent microlens in the 21x21 lens array may ultimately be absorbed in the detector. Additional work will be needed to understand any such scattering paths. We note that regardless of the source of this enhanced coupling, the NEP shown in Figures 10 and 11 is measured with respect to absorbed power, and is thus a measure of the intrinsic detector sensitivity.

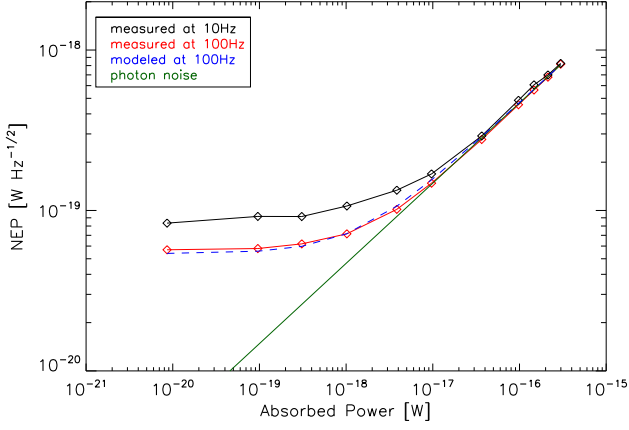


Fig. 10. NEP referenced to absorbed power at sampling frequencies of 10 Hz (*black*) and 100 Hz (*red*), for an estimated optical efficiency of $\eta_{\text{opt}} = 0.9$. Overplotted is the photon NEP (*green*) and a fit to the measured 100 Hz noise combining the photon noise and a fixed contribution added in quadrature (*blue dashed*).

We may also ask to what extent the large inferred optical efficiency may be a consequence of an error in the above analysis. The comparison of the measured NEP_{inc} with the photon-limited NEP_{γ} is valid when the system is photon noise limited, and if this is not the case the extracted η_{opt} will be incorrect. However, there are a number of indications that the detector is indeed photon-noise limited above $P_{\text{abs}} \approx 10$ aW. These include the white shape of the noise PSD (Figure 9), which argues against significant contribution from TLS or other noise sources with a $1/f$ profile, and the large difference between S_{xx} and S_{yy} (Figure 9), which argues against a significant contribution from amplifier noise or any other additive term that may be expected to contribute equally to the noise in both quadratures. We also note that the measured NEP scales as $P_{\text{abs}}^{1/2}$ (Figure 10), as expected for the photon-limited regime (Equation 9). Finally, we note that the optical efficiency is calculated as $\sqrt{\eta_{\text{opt}}} = \text{NEP}_{\gamma}/\text{NEP}_{\text{inc}}$, so an erroneously high η_{opt} is actually the result of the measured NEP_{inc} being lower than expected. Any non-photon noise contribution may be expected to increase NEP_{inc} and reduce the inferred optical efficiency. As such, we consider it much more likely that the detector is indeed simply coupling to the cryogenic blackbody more strongly than expected.

V. KID SENSITIVITY MODEL AND DYNAMIC RANGE

The measurements obtained in Section IV characterize the sensitivity of this detector at $T = 125$ mK and at optical loads up to 300 aW. In this section we use these measurements in a detector model to extrapolate the performance of this detector to higher temperatures and optical loading.

A. KID Model

We use the KID sensitivity model previously developed in Ref. 27, with parameters updated to match the detector measured here. The responsivity model is given by Equations 4 and

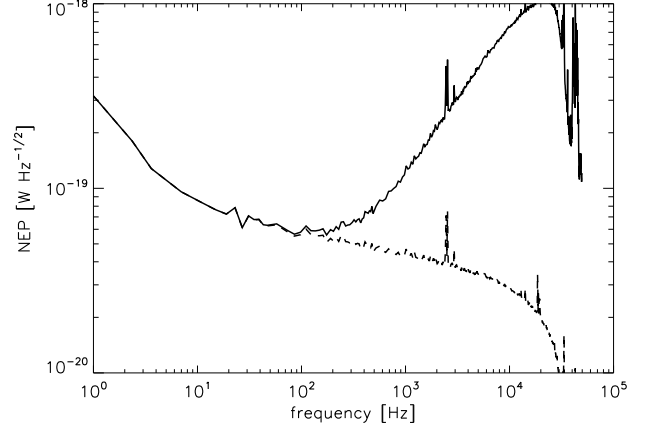


Fig. 11. NEP referenced to absorbed power as a function of sampling frequency measured for an absorbed power $P_{\text{abs}} = 0.0086$ aW, both before correcting for the reduced response at high frequency (*dashed*), and after the correction, assuming $\tau_{\text{qp}} = 415$ μs (*solid*).

5. In Section IV-B we obtained estimates of $R_0 = 7.6 \times 10^{10} \text{ W}^{-1}$ and $P_0 = 35.5$ aW at $T = 125$ mK, where $n_{\text{th}} \ll n^*$, and the $(1 + n_{\text{th}}/n^*)$ term may be set to 1. These estimates also assumed a constant value of $S_2(\omega) = 3.4$. Using $\eta_{\text{opt}} = 0.9$ we extend these results to adopt a responsivity model with finite n_{th} and variable $S_2(\omega)$:

$$\frac{dx}{dP_{\text{abs}}} = \frac{R_0}{\eta_{\text{opt}}} \frac{S_2(\omega)}{3.4} \left[\left(1 + \frac{n_{\text{th}}}{n^*} \right)^2 + \frac{P_{\text{abs}}}{\eta_{\text{opt}} P_0} \right]^{-1/2} \quad (10a)$$

$$= [2.5 \times 10^{10} \text{ W}^{-1}] S_2(\omega) \left[\left(1 + \frac{n_{\text{th}}}{n^*} \right)^2 + \frac{P_{\text{abs}}}{32 \text{ aW}} \right]^{-1/2}. \quad (10b)$$

The model for τ_{qp} developed in Section IV-B may be parameterized with $n^* = 20 \mu\text{m}^{-3}$, and we compute $n_{\text{th}}(T)$ using $\Delta_0 = 0.245$ meV. We calculate $S_2(\omega)$ by assuming a thermal quasiparticle distribution, with an effective temperature obtained by solving $n_{\text{th}}(T) = n_{\text{qp}}$ [27].

It is informative to compare the measured value of $R_0 = 7.6 \times 10^{10} \text{ W}^{-1}$ with a prediction using our best estimates of the fundamental KID parameters in Equation 5. We assume the inductor volume is $V = 20.6 \mu\text{m}^3$, as designed, and make use of the results of Section IV-A to specify $\alpha = 0.95$ and $\Delta_0 = 0.245$ meV. The model for τ_{qp} developed in Section IV-B indicates $\tau_{\text{max}} = 420 \mu\text{s}$, and we adopt a pair-breaking efficiency of $\eta_{\text{pb}} = 0.5$ (Section V-C). These parameters give an expected value of $R_0 = 5 \times 10^{10} \text{ W}^{-1}$, a factor of ≈ 1.5 smaller than measured. Equation 5 is the product of a number of terms, each with their own uncertainty, and we are encouraged that the responsivity computed from the basic detector parameters is close to the measured value. We stress that the responsivity used in this section is based on the measurements in Section IV-B, and not on a first principles detector model.

At low optical loading the electrical noise at 10 Hz is $S_{xx} \approx 5 \times 10^{-17} \text{ Hz}^{-1}$, and is assumed to be dominated by TLS noise (Figure 9). The amplifier noise contribution is

$S_{xx} \approx 3.5 \times 10^{-18} \text{ Hz}^{-1}$, which corresponds to an effective noise temperature of $T_n = 15 \text{ K}$ when referenced to the input of the cryogenic amplifier. We expect this will be improved in the PRIMA readout chain, but conservatively carry this as-measured noise in the analysis below. The scaling of TLS noise, amplifier noise, thermal GR noise, and microwave generation noise with temperature, optical loading, and resonator detuning are all described in Ref. 27.

B. Temperature Dependence

In Figure 12 we show the set of S_{xx} noise measurements obtained at $T = 100 - 275 \text{ mK}$ for the detector in the dark condition, along with a decomposition of the PSD using the fitting function described in Equation 7. At low temperature the noise at 10 Hz is dominated by the TLS component, and the rising thermal GR component is seen to dominate above $T \gtrsim 200 \text{ mK}$. Our corresponding NEP model, which includes the reduced responsivity at higher temperatures, is shown in Figure 13. These figures suggest that the optimal temperature for the PRIMA detectors is about 150 mK, and that they can operate at up to $\approx 175 \text{ mK}$ before starting to suffer from an increasing thermal GR noise.

C. Pair-Breaking Efficiency

Of particular interest in understanding the performance of these KIDs at THz frequencies is estimating what fraction of the absorbed photon energy is ultimately converted to quasiparticles. This is the pair-breaking efficiency η_{pb} , which is typically assumed to be $\eta_{pb} \approx 0.3 - 0.6$ [28], [29], but which is not often measured.

We can estimate this efficiency by comparing the GR noise in two different regimes: i) when the quasiparticle system is in thermal equilibrium, and ii) when there is a strong excess of photo-produced quasiparticles. An examination of Figure 6 shows that the total frequency shift resulting from varying the stage temperature with a fixed optical load is larger than the total frequency shift obtained by varying the optical load at fixed stage temperature. At the same time, Figures 9 and 12 show that the high optical loading measurements produced the most GR noise. This may be understood by noting that the resonator frequency shift is determined by n_{qp} , and that for a given quasiparticle production rate (and hence equilibrium quasiparticle number density), the absorption of high energy photons produces a larger variance in n_{qp} than does thermal fluctuations, because single photons can produce multiple quasiparticles.

In the limit of no optical loading and no readout power dissipation the system is in thermal equilibrium, and the GR noise may be written as [10]:

$$S_{xx,gr} = \left(\frac{\delta x}{\delta n_{qp}} \right)^2 \left[\frac{4 n_{qp} \tau_{qp}}{V} \left(1 + \frac{\tau_{qp}}{\tau_{max}} \right) \right]. \quad (11)$$

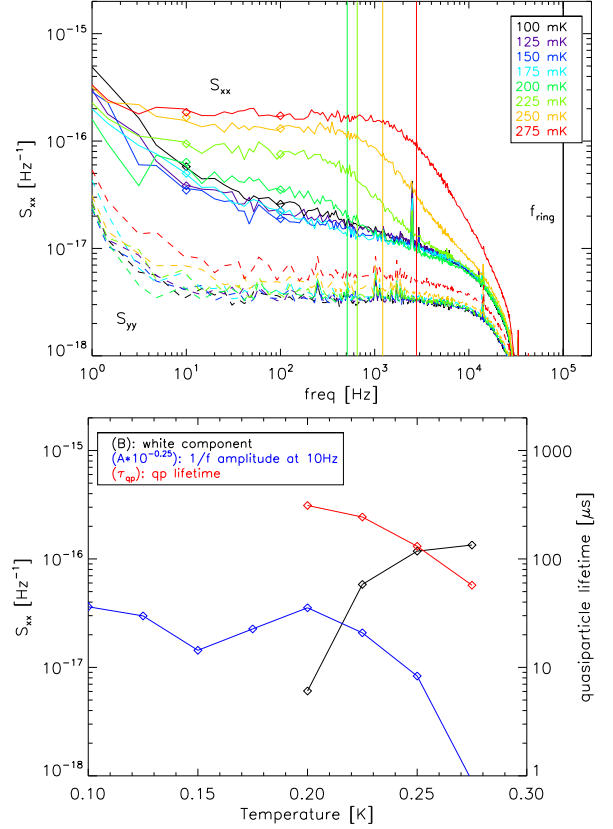


Fig. 12. (top) Fractional frequency noise over a range of stage temperatures, with electrical noise spikes at 60Hz and harmonics removed. Noise in the orthogonal direction shown as dashed lines (S_{yy}). Vertical lines indicate the fitted roll-off of the resonator component, and thick line at 100 kHz indicates the resonator ring-down frequency. (bottom) Fitting results of the PSDs using Equation 7.

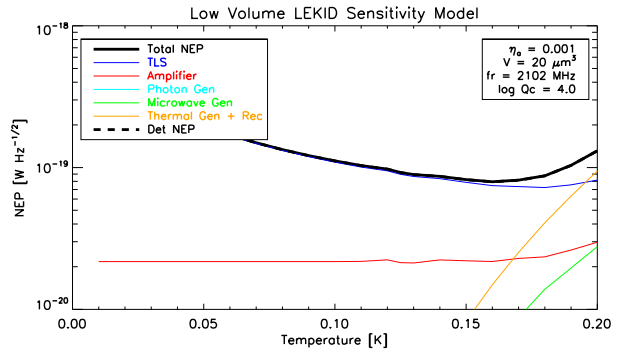


Fig. 13. Modeled 10 Hz NEP as a function of temperature in the low optical loading limit. The TLS-limited NEP dominates at low temperature, while thermal GR noise dominates above $T \gtrsim 200 \text{ mK}$.

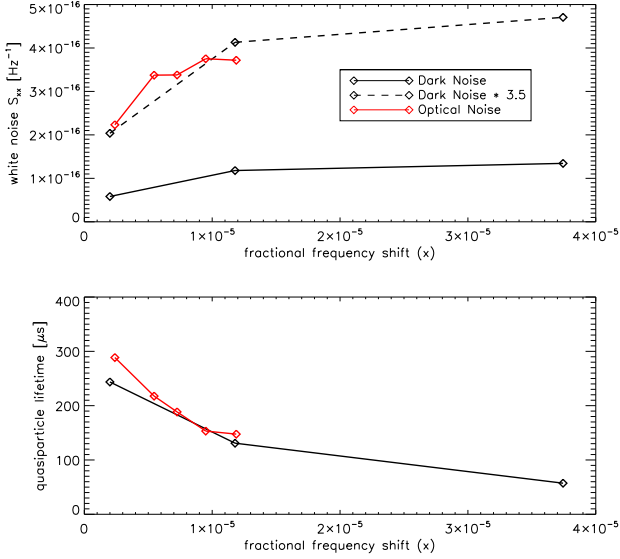


Fig. 14. Comparison of white noise (*top*) and quasiparticle lifetime (*bottom*) under dark stage temperature sweeps and with elevated optical load. For a given fractional frequency shift the GR noise evident under an optical load is ≈ 3.5 times larger than when at elevated stage temperature, while the quasiparticle lifetime is approximately the same in the two regimes.

In the opposite limit, if the quasiparticle population is dominated by photon absorption with little thermal generation, the GR noise may be written as:

$$S_{xx,gr} = \left(\frac{\delta x}{\delta n_{qp}} \right)^2 \left[\frac{4 n_{qp} \tau_{qp}}{V} \left(1 + \frac{\tau_{qp}}{\tau_{max}} \right) \right] \frac{1}{2} \left[\left(\frac{\eta_{pb} h \nu}{2 \Delta_0} \right) (1 + n_0) + 1 \right]. \quad (12a)$$

If we compare the noise measured under an optical load (following Equation 12) with that measured dark (following Equation 11), and take care to conserve n_{qp} , we expect a ratio:

$$R = \frac{S_{xx,optical}}{S_{xx,dark}} = \frac{1}{2} \left[\left(\frac{\eta_{pb} h \nu}{2 \Delta_0} \right) (1 + n_0) + 1 \right]. \quad (13)$$

In the top panel of Figure 14 we compare the white noise level in the two regimes as a function of frequency shift. We see that for a given frequency shift the GR noise under an elevated optical load is ≈ 3.5 times larger than when the frequency shift is due to an increased temperature. The bottom panel compares the quasiparticle lifetime estimated in the two regimes. Here we see that τ_{qp} is much more similar in the two cases, as expected if τ_{qp} and the frequency shift x are both primarily determined by the equilibrium n_{qp} . From Equation 13, we see that a measured ratio of $R = 3.5$ corresponds to $\eta_{pb} = 0.5$ for $\Delta_0 = 0.245$ meV, consistent with the assumption made in this work. This value is somewhat larger than the value of $\eta_{pb} = 0.3$ that we can estimate based on a calculation of the phonon escape time of 0.05 ns for our 30 nm film [30], and the literature value of the pair breaking time of aluminum of 0.26 ns [28].

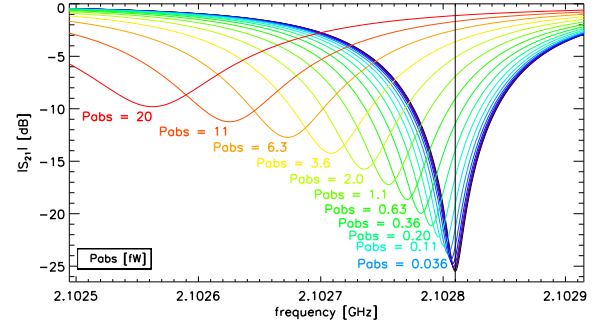


Fig. 15. Simulated transmission profiles for this resonator under increasing optical load, up to an absorbed power of 20 fW. When operating at increased loading the detector is assumed to be biased at a fixed drive power and frequency (vertical black line).

D. In-Orbit Loading and Dynamic Range

The loading for PRIMA's FIRESS spectrometer varies across the full wavelength range, as both pixel size (solid angle) and spectral bin size are subject to optimization. The instrument design prioritizes high efficiency and couples both polarizations, resulting in a per-pixel loading of 2 – 10 aW when viewing low-zodiacal sightlines such as the ecliptic poles. The KIDs can be designed for higher loadings (e.g. for larger spectral bandwidth as designed for PRIMA's imager PRIMAgar) simply by increasing the volume of the inductor. This will reduce the detector responsivity, but increase the maximum optical load under which the detector remains photon-noise limited.

To understand the capability of PRIMA KIDs to measure very bright sources we use our detector model to extrapolate the detector frequency and Q_r response to higher loadings than the maximum power of 300 aW probed here. In Figure 15 we show a set of modeled detector transmission profiles under increasing optical load. To estimate the NEP at each loading value we scale each component in the noise budget following the scalings described in Ref. 27. We assume that the detector is biased with a drive power and tone frequency appropriate for operation in the low loading limit. Importantly, the noise scaling accounts for the fact that the probe tone frequency becomes progressively further detuned from the resonance frequency as the optical loading increases. The modeled noise budget is shown in Figure 16. The detector becomes photon noise limited at an absorbed power of ≈ 5 aW, consistent with the measurements presented in Figure 9. This model predicts that the detector will remain photon noise limited until a loading of ≈ 20 fW. At this point the resonator becomes significantly detuned (Figure 15), and a given fractional frequency shift will have a decreasing impact on the microwave transmission. As the amplifier noise adds to the microwave signal, this noise term begins to dominate. For reference to astronomical sources, PRIMA's FIRESS spectrometer at $\lambda = 100 \mu\text{m}$ has a conversion of 10 milli-Janskys per aW, so the 20 fW power at which amplifier noise becomes dominant corresponds to 200 Jy.

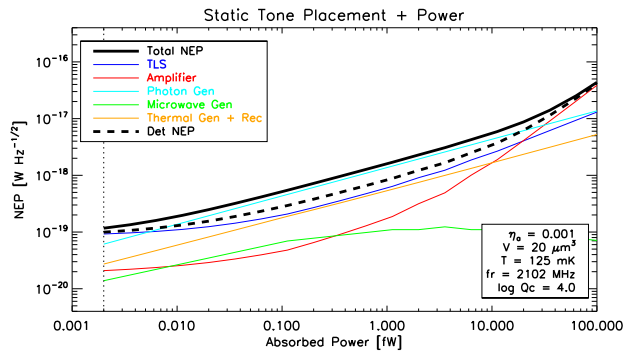


Fig. 16. Modeled 10 Hz NEP as a function of optical loading. The detector is predicted to be photon noise limited above ≈ 5 aW of loading, and remain so until ≈ 20 fW, at which point the amplifier noise becomes dominant. The photon noise curve applies to $\lambda = 210 \mu\text{m}$. At PRIMA's shorter wavelengths there is more shot noise for a given optical load, and we anticipate the short wavelength detectors may remain photon noise limited to yet higher power.

Even larger signals can be accommodated by the PRIMA KIDs. One approach is to simply incur the amplifier noise penalty shown in Figure 16. Alternatively, to recover shot noise limited performance, the readout frequencies can be retuned to more closely match the loaded condition (see Figure 15) – this is envisioned for PRIMA when viewing bright sources. The ultimate limitation for KIDs when retuning is employed is the reduced resonator quality factor and the associated resonator cross-talk, which slowly degrades yield. These are aspects which are under consideration in our array optimization.

VI. SUMMARY

We describe the design, fabrication, and measurement of a far-IR kinetic inductance detector optimized to work at $210 \mu\text{m}$. At low optical loading this detector achieves a noise equivalent power of $9 \times 10^{-20} \text{ W Hz}^{-1/2}$, meeting the sensitivity target for moderate resolution spectroscopy with the proposed PRIMA space mission. The measurements presented here suggest this detector will remain photon noise limited in the $0.005 - 20$ fW loading range, offering the capability of measuring bright astronomical sources. As companion papers describe [5], [12], [18], we are proceeding to fabricate kilopixel arrays based on this detector design, with initial results indicating high yield and success in bonding with lens arrays.

Acknowledgments. We acknowledge useful discussions with Jonas Zmuidzinas. Funding for this work was provided by the National Aeronautics and Space Administration (Grant No. 80NSSC19K0489; PI S. Hailey-Dunsheath). This work was performed in part at the Jet Propulsion Laboratory, California Institute of Technology, under a contract with the National Aeronautics and Space Administration. Copyright 2023 California Institute of Technology. U.S. Government sponsorship acknowledged.

REFERENCES

- [1] A. Moullet, T. Kataria, D. Lis, *et al.*, “PRIMA General Observer Science Book,” *arXiv e-prints*, arXiv:2310.20572 (2023).
- [2] J. Baselmans, J. Bueno, S. J. Yates, *et al.*, “A kilo-pixel imaging system for future space based far-infrared observatories using microwave kinetic inductance detectors,” *Astronomy & Astrophysics* **601**, A89 (2017).
- [3] L. J. Liu, R. M. J. Janssen, C. M. Bradford, *et al.*, “Design of the Kinetic Inductance Detector Based Focal Plane Assembly for the Terahertz Intensity Mapper,” *Journal of Low Temperature Physics* **209**, 953–961 (2022).
- [4] K. Karatsu, A. Endo, J. Bueno, *et al.*, “Mitigation of cosmic ray effect on microwave kinetic inductance detector arrays,” *Applied Physics Letters* **114**, 032601 (2019).
- [5] E. Kane, C. Albert, R. Basu Thakur, *et al.*, “Modeling of cosmic rays and near-IR photons in aluminum KIDs,” *Journal of Low Temperature Physics* (submitted) (2023).
- [6] S. Masi, P. de Bernardis, A. Paiella, *et al.*, “Kinetic Inductance Detectors for the OLIMPO experiment: in-flight operation and performance,” *Journal of Cosmology and Astroparticle Physics* **2019**, 003 (2019).
- [7] I. N. Lowe, P. Ade, P. Ashton, *et al.*, “Characterization, deployment, and in-flight performance of the BLAST-TNG cryogenic receiver,” in *Millimeter, Submillimeter, and Far-Infrared Detectors and Instrumentation for Astronomy X*, J. Zmuidzinas and J.-R. Gao, Eds., SPIE (2020).
- [8] J. Baselmans, S. Yates, P. Diener, *et al.*, “Ultra low background cryogenic test facility for far-infrared radiation detectors,” *Journal of Low Temperature Physics* **167**(3-4), 360–366 (2012).
- [9] J. J. A. Baselmans, F. Facchin, A. Pascual Laguna, *et al.*, “Ultra-sensitive THz microwave kinetic inductance detectors for future space telescopes,” *A&A* **665**, A17 (2022).
- [10] S. Hailey-Dunsheath, A. C. M. Barlis, J. E. Aguirre, *et al.*, “Development of Aluminum LEKIDs for Balloon-Borne Far-IR Spectroscopy,” *Journal of Low Temperature Physics* **193**, 968–975 (2018).
- [11] R. M. J. Janssen, R. Nie, B. Bumble, *et al.*, “Single Pixel Performance of the Kinetic Inductance Detectors for the Terahertz Intensity Mapper,” *Journal of Low Temperature Physics* **211**, 197–206 (2023).
- [12] L. Foote, C. Albert, J. Baselmans, *et al.*, “High-sensitivity Kinetic Inductance Detector Arrays for the Probe Far-Infrared Mission for Astrophysics,” *Journal of Low Temperature Physics* (submitted) (2023).
- [13] P. M. Echtenach, S. van Berkel, A. D. Beyer, *et al.*, “Large Array of Single-Photon Counting Quantum Capacitance Detectors,” *IEEE Transactions on Terahertz Science and Technology* **12**, 211–216 (2022).
- [14] N. Llombart, B. Blazquez, A. Freni, *et al.*, “Fourier Optics for the Analysis of Distributed Absorbers Under THz Focusing Systems,” *IEEE Transactions on Terahertz Science and Technology* **5**, 573–583 (2015).
- [15] N. Llombart, S. Dabironezare, G. Carluccio, *et al.*, “Reception power pattern of distributed absorbers in focal plane arrays: A fourier optics analysis,” *IEEE Transactions on Antennas and Propagation* **66**, 5990–6002 (2018). Accepted Author Manuscript.
- [16] J. Ruzé, “Antenna Tolerance Theory – A Review,” *IEEE Proceedings* **54**, 633–642 (1966).
- [17] T. H. Buttgenbach, “An improved solution for integrated array optics in quasi-optical mm and submm receivers: the hybrid antenna,” *IEEE Transactions on Microwave Theory Techniques* **41**, 1750–1760 (1993).
- [18] N. F. Cothard, T. Stevenson, J. Mateo, *et al.*, “Monolithic kilopixel silicon microlens arrays for future far-infrared observatories,” *Journal of Low Temperature Physics* (submitted), arXiv:2311.00819 (2023).
- [19] M. J. Persky, “Review of black surfaces for space-borne infrared systems,” *Review of Scientific Instruments* **70**, 2193–2217 (1999).
- [20] L. J. Swenson, P. K. Day, B. H. Eom, *et al.*, “Operation of a titanium nitride superconducting microresonator detector in the nonlinear regime,” *Journal of Applied Physics* **113**, 104501–104501–9 (2013).
- [21] J. Zmuidzinas, “Superconducting microresonators: Physics and applications,” *Annual Review of Condensed Matter Physics* **3**(1), 169–214 (2012).
- [22] M. S. Khalil, M. J. A. Stoutimore, F. C. Wellstood, *et al.*, “An analysis method for asymmetric resonator transmission applied to superconducting devices,” *Journal of Applied Physics* **111**, 054510–054510–6 (2012).
- [23] J. Gao, J. Zmuidzinas, A. Vayonakis, *et al.*, “Equivalence of the Effects on the Complex Conductivity of Superconductor due to Temperature Change and External Pair Breaking,” *Journal of Low Temperature Physics* **151**, 557–563 (2008).
- [24] H. McCarrick, D. Flanigan, G. Jones, *et al.*, “Horn-coupled, commercially-fabricated aluminum lumped-element kinetic inductance detectors for millimeter wavelengths,” *Review of Scientific Instruments* **85**(12), 123117 (2014).

- [25] J. Gao, M. Daal, J. M. Martinis, *et al.*, “A semiempirical model for two-level system noise in superconducting microresonators,” *Applied Physics Letters* **92**, 212504 (2008).
- [26] R. M. J. Janssen, J. J. A. Baselmans, A. Endo, *et al.*, “High optical efficiency and photon noise limited sensitivity of microwave kinetic inductance detectors using phase readout,” *Applied Physics Letters* **103**, 203503 (2013).
- [27] S. Hailey-Dunsheath, R. M. J. Janssen, J. Glenn, *et al.*, “Kinetic inductance detectors for the Origins Space Telescope,” *Journal of Astronomical Telescopes, Instruments, and Systems* **7**, 011015 (2021).
- [28] T. Guruswamy, D. J. Goldie, and S. Withington, “Quasiparticle generation efficiency in superconducting thin films,” *Superconductor Science Technology* **27**, 055012 (2014).
- [29] T. Guruswamy, D. J. Goldie, and S. Withington, “Nonequilibrium superconducting thin films with sub-gap and pair-breaking photon illumination,” *Superconductor Science Technology* **28**, 054002 (2015).
- [30] S. B. Kaplan, “Acoustic matching of superconducting films to substrates,” *Journal of Low Temperature Physics* **37**, 343–365 (1979).